

1 WIND-DRIVEN UPWELLING AROUND
2 GROUNDED TABULAR ICEBERGS

Alon A. Stern¹, Eric Johnson¹, David M. Holland¹, Till J.W. Wagner², Peter
Wadhams³, Richard Bates⁴, E. Povl Abrahamsen⁵, Keith W. Nicholls⁵, Anna
Crawford⁶, Jonathan Gagnon⁷, Jean-Eric Tremblay⁷

¹Courant Institute of Mathematical
Sciences, New York University, New York,
New York, USA.

²Scripps Institution of Oceanography,
University of California San Diego, San
Diego, CA, USA

³Department of Applied Mathematics and
Theoretical Physics, University of
Cambridge, Cambridge, UK

⁴University of St. Andrews, Scotland, UK

⁵British Antarctic Survey, NERC,
Cambridge, UK

⁶Department of Geography and
Environmental Studies, Carleton University,
Ottawa, Canada

⁷Laboratoire Jean-Eric Tremblay,
Departement de biologie, Quebec-Ocean,
Universit Laval, Quebec, Canada

3 **Abstract.** Temperature and salinity data collected around grounded tab-
4 ular icebergs in Baffin Bay in 2011, 2012 and 2013 reveal indications of wind-
5 induced upwelling at certain locations around the icebergs. These data sug-
6 gest that along one side of the iceberg, wind forcing creates a Ekman trans-
7 port away from the iceberg, which causes upwelling of the cool saline water
8 from below. The upwelling water mixes with the water in the thermocline,
9 causing the mixed layer to become cooler and more saline. Along the oppo-
10 site side of the iceberg, the surface Ekman transport moves towards the ice-
11 berg, which causes a sharpening of the thermocline as warm fresh water is
12 trapped near the surface. This results in warmer mixed layer temperatures
13 and lower mixed layer salinities. We hypothesize that the asymmetries in wa-
14 ter temperature around the iceberg, caused by the opposing effects of up-
15 welling and sharpening of the thermocline, could lead to differential dete-
16 rioration around the iceberg. Analysis of satellite images indeed reveals dif-
17 ferential disintegration around one of the icebergs, consistent with this mech-
18 anism.

1. Introduction

19 Large icebergs, which calve off outlet glaciers in Antarctica and Greenland, are es-
20 timated to contribute approximately 50 percent of the total freshwater flux from the
21 cryosphere into the global ocean [Rignot et al., 2013]. These massive pieces of ice drift
22 away from their calving origins, directed by winds and currents towards regions with
23 warmer water where they melt, break up and eventually dissolve completely. The trajec-
24 tories and life cycles of the icebergs determine the spatial and temporal distribution of
25 much of the fresh water flux from the cryosphere into the ocean, which is a non-negligible
26 term in the regional fresh water budget [Gladstone et al., 2001; Silva et al., 2006]. This
27 has implications for various processes in the climate system, such as sea-ice distribution
28 and bottom water formation (in Antarctica) [Dinniman et al., 2007; Jongma et al., 2009;
29 Kusahara et al., 2011; Robinson et al., 2012]. As a result, icebergs can affect the iron
30 and nutrient levels locally, leading to the creation of biological hotspots [Kaufmann et
31 al., 2011; Vernet et al., 2011, 2012; Smith et al., 2011; Biddle et al., 2015] and increased
32 sequestration of organic carbon to the deep ocean [Smith et al., 2007; Shaw et al., 2011].

33
34 Modeling iceberg calving and subsequent iceberg trajectories and degradation is tied in
35 with projecting future sea level [Rye et al., 2014]. As a result, recent efforts to couple
36 numerical ocean models to land-ice models have led to an increased interest in Arctic and
37 Antarctic icebergs [Martin and Adcroft, 2010; Hunke and Comeau, 2011; Coogle, 2013].
38 Furthermore, the recent decline in Arctic summer sea ice extent has led to an increased
39 usage of the Arctic for commercial shipping, as well as renewed efforts in hydrocarbon

40 exploration in the region [*Smith and Stephenson, 2013; Hossain and Rao, 2014*]. Finally,
41 the threat that icebergs still pose to ships and offshore structures continues to fuel interest
42 in iceberg trajectories and decay mechanisms [*Halliday et al., 2012; Peterson et al., 2012;*
43 *Turnbull et al., 2015*].

44
45 While some progress has been made towards including icebergs in comprehensive cli-
46 mate models in recent years, model simulations are difficult to constrain because of the
47 scarcity of observational data. As a result, modeled iceberg distributions and trajectories
48 are typically compared with iceberg distribution and trajectory data collected from satel-
49 lite altimetry [*Bigg et al., 1997; Keghouche et al., 2009; Martin and Adcroft, 2010; Hunke*
50 *and Comeau, 2011*]. In-situ measurements of iceberg behavior are much rarer, due to the
51 inherent difficulties of collecting such data. This lack of measurements has hindered our
52 understanding of small-scale processes that affect the iceberg life cycle.

53
54 In this paper, we focus on small-scale processes that affect the decay of grounded ice-
55 bergs, particularly in warm surface waters. Such processes include direct melting, forced
56 convection caused by ocean velocities relative to the iceberg motion [*Savage et al., 2001*],
57 wave-induced flexural stresses [*Wadhams et al., 1983*], and what has been referred to as
58 the “footloose” mechanism [*Wagner et al., 2014*]: increased erosion at the sides of the
59 iceberg due to warm water above the thermocline can lead to the development of an ice
60 foot below the thermocline, which exerts a strong hydrostatic buoyancy force on the edge
61 of the iceberg, and eventually causes the iceberg edge to break off [*Scambos et al., 2005;*
62 *Wagner et al., 2014*].

63

64 The grounding of an iceberg can also significantly affect its decay process. The initial
65 impact caused by an iceberg hitting the sea floor as it runs aground can result in the
66 iceberg breaking up and lead to an overall expedited decay [*Martin et al.*, 2010]. Once
67 grounded, the iceberg will further be subject to increased flexural stresses that are induced
68 by tidal forcing.

69

70 A grounded iceberg will also have an effect on the ocean surrounding it, which in turn
71 can inhibit or enhance iceberg degradation. Firstly, the meltwater from (grounded or
72 ungrounded) icebergs has the potential to either stabilize or destabilize the water col-
73 umn depending on the local hydrography [*Neshyba*, 1977; *Donaldson*, 1978; *Gladstone et*
74 *al.*, 2001; *Kubat et al.*, 2007]. Buoyant subsurface meltwater can rise up the side of the
75 iceberg either as a thin boundary layer, spreading a cool fresh water layer on the ocean
76 surface [*Helly et al.*, 2011], or as a density plume, entraining ambient water, and result-
77 ing in density anomalies throughout the upper water column [*Stephenson et al.*, 2011].
78 The sign of this density anomaly depends on the ambient stratification and the amount
79 of entrainment [*Jenkins*, 1999]. Alternatively, a neutrally buoyant meltwater plume can
80 spread horizontally at depth, causing steps in the temperature and salinity profiles, which
81 are maintained by the effects of double diffusion [*Huppert and Turner*, 1998; *Stephenson*
82 *et al.*, 2011].

83

84 Grounded icebergs also affect the surrounding ocean by disrupting flow, thereby chang-
85 ing the general circulation patterns around the iceberg [*Nøst et al.*, 1998; *Grosfeld et al.*,

2001; *Robinson et al.*, 2010]. In this way, grounded icebergs can act in a similar fashion to islands that are temporarily placed in the flow. Much work has been done on the effect of flow disruptions, wake vortices and upwelling/downwelling caused by the presence of small islands [e.g., *Takahashi et al.*, 1980; *Wolanski et al.*, 1996; *Dietrich et al.*, 1996; *White et al.*, 2008]. It stands to reason that some of the insights gained through this work can be applied to the study of the circulation patterns around temporarily grounded icebergs. Of particular relevance here is the wind-driven upwelling and downwelling that is commonly observed along coastlines of continents and islands [*Garvine*, 1971; *Takahashi et al.*, 1980; *De Szoeke and Richman*, 1981; *Bakun*, 1990; *Kämpf et al.*, 2005, and others]. Coastal upwelling occurs when wind-driven currents are directed offshore and are replenished by water from below. Such upwelling is often associated with increased biological productivity, as nutrient-rich water is brought to the surface [*Hutchins and Bruland*, 1998; *Botsford et al.*, 2003, 2006]. Similarly, coastal downwelling occurs when wind-driven onshore surface currents cause surface water to pile up against the coast and are forced downwards. In the northern hemisphere, the surface Ekman transport is 90 degrees to the right of the prevailing wind direction [*Ekman*, 1905; *Price et al.*, 1987]. A northward wind along the east coast of a land mass, for example, will drive an eastward Ekman transport away from the coast, and result in upwelling. Changes to the prevailing wind direction drive changes in the upwelling signal after some adjustment time [*Send et al.*, 1987].

105

In this study, temperature and salinity measurements are presented from the water columns surrounding two grounded tabular Arctic icebergs, collected over three field seasons. These data suggest that a grounded iceberg can experience upwelling on one side of

109 the icebergs and a sharpening of the density gradients at the base of the thermocline on the
110 opposite side. Amongst other things, this upwelling and thermocline gradient sharpening
111 affects the temperature of the thermocline around the iceberg, which has implications
112 for the eventual iceberg decay. The observed upwelling is driven by surface winds and is
113 distinct from the previously observed upwelling along the sides of an iceberg driven by
114 buoyant meltwater plumes [*Neshyba, 1977; Helly et al., 2011; Stephenson et al., 2011*].

115 This article is organized as follows: section 2 discusses details of the three field ex-
116 periments and the instruments and methods used to collect and analyze ocean data. In
117 section 3, conductivity, temperature and depth (CTD) measurements are used to indicate
118 the presence of upwelling regions and regions of enhanced stratification on opposing sides
119 of the icebergs. In section 4, we suggest that the increased surface water temperatures in
120 the enhanced stratification regions may lead to an increased rate of iceberg degradation
121 on one side of the iceberg. Section 5 contains some concluding remarks.

122

123 Note that in the Arctic, large tabular icebergs are commonly referred to as ‘ice islands’,
124 however in this article we will use the term icebergs instead.

125

2. Methods

2.1. Description of field work

126 Peterman Ice Island (PII) calved off Petermann Glacier in northwest Greenland on 8
127 August 2010. At the time of calving, PII had a surface area of 253 km² and was the
128 largest Greenlandic calving event on record [*Falkner et al., 2011*]. Within a month of
129 calving, two large collision events caused PII to split into 4 parts, the largest of which

130 was PII-B. On 26 October 2010, three smaller fragments calved off of PII-B. These were
131 named PII-B-a, PII-B-b and PII-B-c. The collision and fracture events were observed
132 using RADARSAT-2 satellite imagery. After these fracture events, the remainder of PII-
133 B continued to drift southwards along the western edge of Baffin Bay before becoming
134 grounded on the continental shelf of Baffin Island on 18 June 2011, at $69^{\circ}38'N$, $65^{\circ}52'W$,
135 130 km south east of Clyde River. Figures 1 shows the grounding position of PII-B, as
136 well as (a) the regional and (b) the local bathymetry around the iceberg.

137

138 PII-B was first visited in October 2011. At this time, the iceberg had a surface area of
139 60 km^2 . Ocean CTD data were collected around PII-B on 20 October 2011. Three CTD
140 casts were collected on both the southern side of the iceberg (200 m, 400 m and 600 m
141 away from the iceberg edge) and the northern side of the iceberg (200 m, 300 m and 400
142 m away from the iceberg edge). One cast was collected on both the western and eastern
143 sides of the iceberg, at approximately 300 and 400 m from the iceberg edge, respectively.
144 During this expedition, wind data were collected in situ by a wind monitor positioned on
145 the mast of the ship ~ 15 m above the water line, which was later corrected for the ship
146 motion. The ship path around the iceberg and position of the CTD casts are shown in
147 Figure 6c.

148

149 On 13 November 2011, PII-B split into two parts. The smaller part, PII-B-2, became
150 ungrounded and drifted southwards, and the larger part PII-B-1 remained grounded on
151 the continental shelf at the same location. PII-B-1 was visited for a second time in
152 July 2012 as part of a wider field campaign performed in conjunction with the British

153 Broadcasting Corporation (BBC). The field campaign aimed to study the degradation of
154 icebergs in warm surface water. Results from this field campaign are presented in the
155 BBC television documentary *Operation Iceberg*, and also in *Wagner et al.* [2014]. At this
156 time, PII-B-1 had a surface area of $\sim 42 \text{ km}^2$.

157

158 During this second visit a more comprehensive CTD survey was performed around the
159 iceberg. Temperature, salinity and pressure data were collected using an ADM mini CTD
160 probe with temperature, conductivity, pressure, and dissolved oxygen sensors. The CTD
161 survey was organized in 5 groups which began $< 1 \text{ km}$ from the iceberg edge and moved
162 radially outwards to $\sim 10 \text{ km}$ from the iceberg edge, sampling at approximately logarithmic
163 spacing. These five groups are referred to as Group 1 to Group 5 throughout this
164 study. The location, time and ocean depth of each CTD casts is shown in Figures 1c, 1d
165 and 1e, respectively. A further CTD profile was collected within a few centimeters of the
166 iceberg wall using an Idronaut Ocean Seven 320 CTD. This CTD was hand carried by
167 human divers who dived to a depth of 18 meters keeping the CTD as close to the side of
168 the iceberg as possible.

169

170 A Doppler current meter was used to make current measurements at three different depths
171 (5, 50, and 100 m), using bottom tracking when in range. GPS location data were logged
172 separately by the bridge electronic chart display computer. A GPS sensor and logger were
173 placed on the iceberg from 30 July 2012 to 3 August 2012 to monitor the iceberg motion.
174 The iceberg side above the waterline was scanned with an Optec lidar, and the iceberg
175 side beneath the waterline was mapped using a Reson SeaBat 8125 455-kHz multibeam

176 sonar, mounted on a vertical pole next to the hull (see *Wagner et al.* [2014] for more
177 details). The average thickness of the iceberg was ~ 70 m. The positions of the iceberg
178 on 12, 24, and 28 July 2012 are shown in Figure 1b. These iceberg outlines were traced
179 from images recorded by the Moderate Resolution Imaging Spectroradiometer (MODIS)
180 sensor on the NASA Terra satellite.

181

182 One further CTD survey was performed on 10 August 2013 around PII-B-a, one of the
183 aforementioned smaller fragments that split off of PII-B. On 10 August 2013, PII-B-a had
184 a surface area of 8.4 km^2 (measured using RADAESAT-2 images), and was grounded at
185 $71^\circ 20' \text{N}$, $71^\circ 02' \text{W}$ (Figure 1a). CTD measurements were made around PII-B-a using a
186 moving vessel profiler (MVP). The MVP circled the iceberg, remaining 50-100 m from
187 the iceberg edge, and performing 61 dives. The path and dives of the MVP around the
188 iceberg are shown in Figure 7c.

189

190 Information about the accuracy of instruments used in all three field campaigns are re-
191 ported in Table S1. CTD data were processed using TEOS-10 Oceanographic Toolbox
192 [*McDougall and Barker*, 2011]. All conductivity measurements have been converted to
193 absolute salinity (units of g/kg), and all densities are sigma-0. The results below focus
194 on the measurements made around iceberg PII-B-1 in July 2012. Results from the 2011
195 and 2013 campaigns are presented in support of the main findings.

196

2.2. Integrated fresh water and heat content

197 In our analysis below, we make use of the integrated fresh water content and integrated
198 heat content of a given cast, defined as

$$200 \quad F = \int_h^0 [S(z) - S_0] dz, \quad (1)$$

201 and

$$202 \quad H = \int_h^0 [T(z) - T_0] dz, \quad (2)$$

203 respectively. Here $T_0 = -1.71^\circ\text{C}$ and $S_0 = 33.63 \text{ g/kg}$, are the minimum temperature and
204 maximum salinity found across all casts in the July 2012 ocean survey. We use $h = -80$
205 m as the integration depth, chosen as a depth at which all casts are at least 10 m above
206 the bottom. At the depth $h = -80$ m, the temperatures and salinities were approximately
207 equal across all casts. The results using F and H are not sensitive to the choice of h and
208 were qualitatively similar for h in the range $-85 \text{ m} < h < -35 \text{ m}$.

2.3. Diagnostic for upwelling/downwelling wind direction

210 We introduce the quantity $C(t, \phi)$ which indicates whether a particular wind direction
211 is expected to cause upwelling or downwelling offshore of the iceberg. $C(t, \phi)$ is defined
212 as

$$213 \quad C(t, \phi) = \frac{1}{\Delta t} \int_{t-\Delta t}^t u(\phi + 90^\circ) dt \quad (3)$$

214 where

$$215 \quad u(\phi) = \mathbf{u} \cdot \langle \cos \phi, \sin \phi \rangle \quad (4)$$

216 is the component of the wind in the direction ϕ , \mathbf{u} is the wind velocity vector, and ϕ is
217 defined as the outward direction from the center of mass of the iceberg measured in degrees
218 counterclockwise from due east (see Fig 7c, for example). Since the Ekman transport in
219 the northern hemisphere moves 90 degrees clockwise of the wind direction, $u(\phi + 90^\circ)$
220 gives a measure of the amount of offshore Ekman transport we expect in a direction ϕ , for
221 a given wind, \mathbf{u} . $C(t, \phi)$ is the time-average of $u(\phi + 90^\circ)$ over the period $\Delta t = 24$ hours
222 preceding time t , and therefore gives a measure of whether on average the wind has been
223 in a direction consistent with upwelling or downwelling over the last 24 hours.

3. Results

3.1. Rotation of PII-B-1 around a pivot point

224 A time series of the location of the GPS, deployed on PII-B-1 from 30 July 2012 to 3
225 August 2012, shows the iceberg moving back and forth across the arc shown in Figure
226 1b (the time series is not shown). Current data collected simultaneously show that the
227 current is dominated by a barotropic diurnal tide. The on-ice GPS was observed to move
228 back and forth, along the arc traced in Figure 1b, with the motion being almost perfectly
229 in-phase with the tidal motion. Completing the circle from the arc of the GPS record
230 reveals the approximate location of the pivot point, marked with a star on Figure 1b.
231 This location corresponds to a topographic rise observed in the IBCAO V3 [*Jakobsson*
232 *et al.*, 2012] bathymetry data set, and is positioned close to the shallowest bathymetry
233 observed using the ship's sonar (92 m). MODIS images of the iceberg from 12 July 2012
234 to 28 July 2012 are consistent with the iceberg pivoting around the indicated pivot point
235 (Figure 1b). From this we infer that one end of the iceberg was grounded on a shallow
236 topographic rise, and the other end was pivoting back and forth with the tides creating

237 the arc observed in Figure 1b. Between 12 July 2012 and 28 July 2012, the iceberg rotated
238 anti clockwise around the pivot point by $\sim 180^\circ$, presumably driven by wind and mean
239 surface currents.

3.2. Melting and meltwater

240 An estimate of the melt rates on the surface, sides and base of PII-B-1 is calculated
241 using energy balance arguments together with in situ ocean data, as well as atmospheric
242 conditions taken from European Centre for Medium-Range Weather Forecasts (ECMWF)
243 daily ERA-Interim reanalysis fields [Dee *et al.*, 2011]. Details of this calculation and a
244 discussion of possible sources of error are given in the supplementary materials. A time
245 series of the volume of meltwater from the surface, sides and base of PII-B-1 over a six
246 month period from March to August 2012 is presented in Figure ??.

247
248 The melt rate estimates suggest that a relatively small amount of melting takes place
249 at the base of the iceberg. This implies that upward motion due to buoyant meltwater
250 production beneath the iceberg is likely to have a small effect on the surrounding ocean.
251 This result was partially confirmed using a neutrally buoyant colored dye, released by
252 human divers along the sides of the iceberg at 18 m below the surface. The dye showed
253 little evidence of upward motion, which indicated the absence of an upward buoyancy
254 current along the sides of the iceberg. Video footage of the dye being released along the
255 side of the iceberg can be viewed at <http://www.bbc.co.uk/programmes/p010jw6w>.

256
257 The largest contribution to the melt rate was from the sides of the iceberg where warm
258 surface temperatures and wave energy cause the formation of a “wavecut” in the iceberg

259 near the waterline, leading to the collapse of the over-hanging ice. The erosion at the
260 sides of the iceberg occurs almost exclusively above the thermocline since (a) the surface
261 water is warmer than water at depth, and (b) surface waves cause increased turbulent
262 exchange between the water and the iceberg. The erosion at the sides of the iceberg is
263 greatly enhanced during summer when the sea ice clears, as the absence of sea ice allows
264 the surface waters to warm and also allows increased wave motion [*Bigg et al.*, 1997].
265 The large amount of near-sea level erosion at the sides of the iceberg suggests that the
266 footloose mechanism is likely to be a significant contributor to the iceberg degradation
267 for PII-B-1 [*Wagner et al.*, 2014]. Melting on the surface of the iceberg makes the second
268 largest contribution. Surface runoff water was observed to flow into the ocean through
269 channels which develop on the iceberg.

270

271 Despite the substantial volume of fresh water entering the ocean via melting of the sides
272 and surface of the iceberg, the meltwater does not appear to have a large effect on the sur-
273 rounding water. The influence of meltwater can be detected by looking at the mixing lines
274 on a T-S diagram. A straight line on a T-S diagram indicates the mixing of two distinct
275 water masses which can be described by the properties at the ends of the mixing line. The
276 presence of meltwater from subsurface melting has been shown to result in a T-S mixing
277 line, known as “Gade line”, which can be extended to the point $(T, S) = (\sim -L/c_p, 0)$
278 [*Gade*, 1979]. Here L is the latent heat of fusion of ice, and c_p is the specific heat of water.
279 For ice melted by the atmosphere, the latent heat is given off into the atmosphere, so the
280 influence of runoff meltwater can be detected by the presence of a mixing line which can
281 be extended to the point $(T, S) = (T_f, 0)$. Here $T_f = 0^\circ\text{C}$ is the freezing point of fresh

282 water.

283

284 Figure 2a and Figure 2b show two typical examples of T-S diagrams from CTD casts
285 taken during the 2012 experiment (the temperature and salinity profiles are shown in the
286 insets). In both figures (as well as for almost all other casts), the mixing lines have a
287 negative gradient, indicating that they are not strongly influenced by meltwater. Figure
288 2c shows the results of a CTD cast taken within a few centimeters of the iceberg wall.
289 Again we see very little evidence of meltwater. The absence of meltwater in these panels
290 suggests that the ocean is very efficient at mixing meltwater with the ambient water. This
291 result stands in contrast to some other observations around free-floating icebergs which
292 have detected a strong presence of meltwater in the surrounding ocean [*Stephenson et al.*,
293 2011; *Helly et al.*, 2011]. This discrepancy may be due to the grounded iceberg being
294 subject to stronger relative ocean currents, compared to a free-floating iceberg, which
295 causes increased rates of mixing between the melt water and the surrounding ocean.

296

297 A strong meltwater signal was seen in just two of the 38 casts (Cast 11 and Cast 12,
298 Group 2). Figure 2d shows the T-S diagram for Cast 11. The “runoff” mixing line with
299 positive gradient can be extended approximately to the point $(T, S) = (T_f, 0)$, which
300 indicates the presence of surface runoff. This cast was taken 1 km from the side of the
301 iceberg. The meltwater from the surface of the iceberg runs off the iceberg in rivers which
302 input most of the meltwater into the ocean at a few discrete spots. It is likely that Cast
303 11 was taken near one of these rivers, which would explain why so much meltwater was
304 detected. The “runoff” mixing line in Figure 2d is notably distinct from the Gade line,

305 indicating that the meltwater was not created by subsurface melting.

306

307

3.3. Ocean conditions around PII-B-1

3.3.1. Asymmetries in mixed layer temperature and salinity around PII-B-1

309 CTD profiles collected around PII-B-1 from 25 July 2012 to 29 July 2012 show substan-
310 tial variations in the mixed layer temperatures and salinities at different points around
311 the iceberg. In general, surface water was observed to be ~ 2 degrees warmer and ~ 3
312 g/kg fresher on the southern and western side of the iceberg than on the eastern side.
313 Most of the temperature and salinity differences occurred in the top 30 m of the water
314 column, while relatively little variation was observed at depths below 30 m. For example,
315 the temperature and salinity profiles of Cast 13, collected on the northwestern side of the
316 iceberg, and Cast 27, collected on the eastern side, are shown in the insets of Figures
317 2a and 2b, respectively. Cast 13 has a surface temperature and salinity of $\sim 6^\circ\text{C}$ and
318 $\sim 27\text{g/kg}$, respectively, while the surface temperature and salinity of Cast 27 are $\sim 4^\circ\text{C}$
319 and $\sim 30\text{g/kg}$, respectively.

320

321 The asymmetries around the iceberg can be clearly seen when the casts are divided
322 into the five groups, based on their orientation around the iceberg. Figures 3a-e show
323 temperature sections for the upper 30 m of the water column in Groups 1 to 5, respec-
324 tively, with density contours overlain (the density is dominated by the effect of salinity).
325 The horizontal axis represents distance from the iceberg edge, and the vertical axis depth
326 below sea level. Figure 3f shows an interpolation of the ocean temperature 5 m below

327 the surface. Figure 4 is analogous to Figure 3, giving the corresponding salinity profiles.
328 Overall, the profiles show a warm fresh water layer in the upper ocean. Below this layer,
329 there is a sharp transition to the cooler salty waters below. The upper ocean is warmest
330 and freshest in Groups 1 and 2 (collected on the south and west of the iceberg, respec-
331 tively), while temperatures are lower and salinities are higher in Groups 4 and 5 (collected
332 to the northeast and southeast of the iceberg, respectively). The isopycnals at the base
333 of the thermocline are mostly flat in Groups 1 and 2 (Figures 3a,b). In Groups 4 and 5,
334 by contrast, the isopycnals at the base of the thermocline are tilted upwards towards the
335 iceberg (Figures 3d,e), suggesting the presence of upwelling on this side of the iceberg.
336 Groups 1 and 2 have a very sharp temperature and density transition at the base of the
337 thermocline, while the transition in Groups 4 and 5 is much more gradual. Group 3
338 (collected on the northern side of the iceberg) is an intermediate case which shares some
339 properties with Group 1 and 2, and some with Groups 4 and 5, as discussed below.

340

341 Similar asymmetries in the mixed layer salinity and temperature to those of the 2012
342 data are observed in the data collected around PII-B in October 2011 and around PII-B-a
343 in August 2013. Figures 6a and 6b, and Figures 7a and 7b show the temperature and
344 salinity sections around PII-B and PII-B-a, with density contours overlain. The horizontal
345 axis in all four panels gives the angle of rotation around the icebergs, measured counter-
346 clockwise from due east, using the center of the icebergs as a reference. The vertical axis
347 is the depth below sea level. Figures 6a and 6b show the presence of warmer and fresher
348 water on the west of PII-B, and cooler, more saline water to the east. The deepening of
349 the base of the thermocline on the western side of the iceberg, suggest the presence of

350 downwelling in this region. Figures 7a and 7b, show anomalously cool and saline water
351 on the western side of PII-B-a, compared to the warmer fresher water on the eastern side.
352 The shoaling of the base of the thermocline on the west on PII-B-a suggest the presence
353 of upwelling in this region.

354

355 **3.3.2. Vertical mixing around PII-B-1**

356 The extent of vertical mixing around the PII-B-1 can be inferred by considering the
357 mixing lines in the T-S diagrams around the iceberg. Figure 2a (Cast 13 in Group 2) has
358 two visible mixing lines, indicating that there is vertical mixing above and below the base
359 of the thermocline, but little vertical mixing between the water at depth and the water
360 in the thermocline. In contrast, Figure 2b (Cast 27 in Group 4) has just one mixing line
361 indicating water from below the thermocline mixes to the surface. The single mixing line
362 on the T-S diagram of Cast 27 is similar to all casts in Groups 4 and 5, and suggests
363 that the colder, more saline water found in the mixed layer in these two groups, is caused
364 by upwelling of cool, saline water from below. The two separate mixing lines in the T-S
365 diagram of Cast 13 is typical of all casts in Groups 1 and 2, and suggests that warmer
366 fresher water is trapped near the surface.

367

368 **3.3.3. Evidence of an overturning circulation**

369 Figure 5a shows the integrated freshwater content, F (defined in section 2.2), for each
370 cast, and how it varies with distance from the iceberg. The freshwater content is consis-
371 tently larger in Groups 1 and 2 than in Groups 4 and 5. Since F is a vertically integrated
372 quantity, this implies that the asymmetries observed around the iceberg are not formed by

373 vertical mixing alone, but rather require some horizontal advection to supply or remove
374 fresh water from the water column. The fresh water content, F , decreases with distance
375 to the iceberg in Group 2 and remains broadly constant in Group 1. In Groups 4 and 5,
376 by contrast, F increases with distance from the iceberg. Similarly, Figure 5b shows that
377 the integrated heat content of the water column, H , mostly increases with distance from
378 the iceberg in Groups 4 and 5, while the behavior is less clear in Groups 1 and 2. The
379 fact that the coolest, most saline water is found close to the iceberg in Groups 4 and 5,
380 suggests that the strongest upwelling occurs close to the iceberg, and decreases in strength
381 as one moves radially outwards. This suggest the presence of an overturning cell on the
382 eastern side of the iceberg: cool dense water is advected towards the iceberg at depth,
383 when it reaches the iceberg it upwells to the surface, and then is transported away from
384 the icebergs by surface currents. This causes the isopycnals in Group 4 and 5 to slant
385 upwards, F and H to be smallest close to the iceberg, and mixing lines to extend to the
386 surface. Conversely, in Groups 1 and 2, results suggest that warm fresh water is advected
387 towards the iceberg at the surface. Since the surface water is much less dense than the
388 water below the thermocline, the surface water does not mix easily with the water below
389 it. This causes the warm surface water in Groups 1 and 2 to pile up against the iceberg,
390 and results in the large values of F and H close to the iceberg and large density gradients
391 at the base of the thermocline observed in Groups 1 and 2.

392

393 Figure 5c shows the maximum vertical density gradient at the base of the thermocline,
394 and how it varies with distance from the iceberg. The maximum vertical density gra-
395 dient is largest for Groups 1 and 2 and smaller for Groups 4 and 5, as expected from

396 the discussion above. In Groups 1 and 2, the maximum vertical density gradient at the
397 base of the thermocline mostly decreases with distance from the iceberg, while in Groups
398 4 and 5, the gradient increases somewhat with distance from the iceberg. This again
399 suggests that the strongest upwelling is occurring close to the iceberg in Groups 4 and 5,
400 and that warm fresh surface water is being advected towards the iceberg in Groups 1 and 2.

401

402 As mentioned before, Group 3 is an intermediate group that shares certain properties
403 with Groups 1 and 2, and other properties with Groups 4 and 5. The mixed layer in
404 Group 3 is relatively warm and fresh, and is similar to that of Groups 1 and 2. This
405 results in large values for the integrated fresh water content, F , and integrated heat con-
406 tent, H , in Group 3. However, the density gradients at the base of the thermocline in
407 Group 3 are not as sharp as in Groups 1 and 2, and some of the isopycnals slope upwards
408 towards the iceberg, as in Groups 4 and 5. A possible explanation is that Group 3 is in a
409 transitional state, transitioning from having enhanced stratification (as in Groups 1 and
410 2) to having ocean upwelling (as in Groups 4 and 5).

411

412 **3.3.4. Wind-driven upwelling and downwelling**

413 Based on these findings, we propose that asymmetries in the temperature, salinity, and
414 depth of the mixed layer around PII-B-1 were caused by wind-driven upwelling and wind-
415 driven enhanced stratification of the thermocline that occurred on opposite sides of the
416 iceberg. This wind-induced upwelling is analogous to wind-driven coastal upwelling. In
417 the case of a grounded iceberg, the iceberg acts in place of the land mass, and allows
418 for upwelling to occur when the offshore direction is to the right of the prevailing wind

419 direction. According to this mechanism, the wind forces the surface waters away from the
420 iceberg on one side of the iceberg, which allows for upwelling water from below to move
421 to the surface. On the other side of the iceberg, the wind drives the surface water towards
422 the iceberg. Since the surface water is much less dense than the water below, the surface
423 water does not mix easily with the water below it, and warm fresh water piles up against
424 the iceberg causing a sharpening of the density gradients at the base of the thermocline
425 on this side of the iceberg. A schematic of this mechanism is shown in Figure 8.

426

427 To test whether the asymmetries in the collected ocean data could have indeed been
428 caused by such a wind-driven mechanism, we consider the ERA-Interim reanalysis wind
429 data for the 2012 observation period, since no wind data was collected in situ. Figures
430 9b and 9c show the wind direction and wind speed, respectively, at the location of the
431 iceberg from 25 July 2012 to 30 July 2012. Figure 9a is a Hovmöller diagram of the quan-
432 tity $C(t, \phi)$, defined in section 2.3. Positive values of $C(t, \phi)$ imply winds consistent with
433 upwelling in the offshore direction ϕ , and negative values of $C(t, \phi)$ imply winds consistent
434 with downwelling in the offshore direction ϕ , which would caused enhanced stratification
435 at the base of the thermocline in this direction. The position and time of the CTD casts
436 have been plotted onto Figure 9a. The angle of each cast was calculated using the center
437 of the iceberg as a reference. Figure 9a shows that the CTD casts in Groups 1 and 2
438 were collected after a period where the wind was consistent with downwelling (causing a
439 sharpening of the thermocline), and casts in Groups 4 and 5 were collected after a period
440 where the wind was consistent with upwelling. Group 3's casts were collected after a
441 short period of weak upwelling winds, however we also observe that the wind direction

442 had change from downwelling winds to upwelling winds approximately one day before the
443 casts were collected. These results therefore support the upwelling/enhanced stratifica-
444 tion mechanism described above.

445

446 Figures 6d and Figure 7d show Hovmöller diagrams of $C(t, \phi)$, for the wind around iceberg
447 PII-B in October 2011, and PII-B-a in August 2013, respectively. Figure 6d is computed
448 from wind data collected in situ as discussed in section 2.2, while Figure 7d again uses
449 ERA-Interim reanalysis wind data. In Figure 6d we see that the deepening of the ther-
450 mocline on the west of the iceberg (blue dot) occurs after winds which are consistent with
451 a downwelling. In Figure 7d we observe that the shoaling of the base of the thermocline
452 to the west of the PII-B-a (red dots in Figure 7) occurs after winds which are consistent
453 with a upwelling.

454

455 **3.3.5. Other factors that could influence the ocean temperature and salinity** 456 **around the iceberg**

457 Current data collected using the Doppler current meter at 5 m, 50 m and 100 m show
458 that the current is dominated by a barotropic diurnal tide. Figure ?? in the supplemen-
459 tary material shows the zonal, and meridional ocean current at 5 m below the surface.
460 The output of the AOTIM5 tidal model [*Padman and Erofeeva, 2004*] is also shown in
461 Figure ??, and appears to covary with the observed ocean currents. Figure ?? suggests
462 that the asymmetries around the iceberg described above are unlikely to have been caused
463 by the CTD casts having been collected at different phases of the tidal cycle. For example,
464 Groups 4 and 5, which are adjacent groups, both showed warmer, fresher surface water,

465 and yet were collected at different phases in the tidal cycle. Conversely, Groups 2 and 5,
466 which are on opposite sides of the iceberg, were collected at similar phases of the tidal
467 cycle and yet have different surface water properties.

468

469 In section 3.2 we saw that little evidence of meltwater was detected in the CTD casts
470 around PII-B-1. This suggests that the meltwater of the iceberg does not play a signif-
471 icant role in setting the overall temperature and salinity structure of the water around
472 the iceberg. The melt rate estimates show that relatively little meltwater is produced
473 from below the iceberg (Figure ??), which suggests that the upwelling is not driven by
474 subsurface melt plumes. Furthermore, there is no good reason to expect that there should
475 be subsurface melt plumes on one side of the iceberg only, driving upwelling on only one
476 side of the iceberg. The fact that the surface water is both warmer and fresher in Groups
477 1 and 2 than in Groups 4 and 5, again suggests that the differences between the different
478 groups can not be attributed to the influence of runoff meltwater mixing with the surface
479 waters, which would cool and freshen the surface water.

480

481 Figure 5d shows the relationship between the vertically integrated freshwater content,
482 F , and the vertically integrated heat content, H , for the different casts. F and H are
483 positively correlated with one another with a correlation of $r=0.785$, significant to the 99
484 percent confidence level. The strong positive correlation between F and H implies that
485 the asymmetries in temperature and salinity are unlikely to have been caused by surface
486 heat fluxes and fresh water fluxes, which are unlikely to be so well correlated. This sug-
487 gests that the asymmetries around the iceberg were not caused by changing atmospheric

488 conditions during the course of the CTD survey.

489

490 The rotation of PII-B-1 during the CTD survey is a complicating factor in analyzing
491 these data. However, it is not clear how the rotation of the iceberg could have caused
492 the asymmetries observed in the mixed layer temperature and salinity. Since the iceberg
493 rotated with the barotropic tide, it is likely that that the motion of the iceberg caused
494 barotropic changes to the water column. The fact that the phase of the tidal cycle does
495 not appear to have caused the upwelling suggests that the tidal motion of the iceberg is
496 unlikely to have played a central role in these processes.

497

4. Differential iceberg deterioration

498 In the previous sections, we argued that wind-induced upwelling and wind-induced
499 enhanced stratification on opposing sides of a grounded iceberg can result in large asym-
500 metries in surface temperatures around the iceberg. This suggests that the predominant
501 wind patterns may play a central role in the degradation of the iceberg. In particular, on
502 the side of the iceberg where the stratification at the base of the thermocline is enhanced,
503 warmer thermocline temperatures would lead to increased iceberg degradation near sea
504 level, and as a knock-on effect, to expedited decay through the footloose mechanism.

505

506 To test this idea, we consider the degradation of PII-B-1 from 8 January 2012 through 1
507 August 2012. The iceberg's perimeter was digitized from four successive RADARSAT-2
508 Fine-Quad (8 m resolution) images, acquired during this period. Since the iceberg was
509 pivoting on a point of shallow bathymetry where it was grounded, the shapefiles were

510 manually corrected for rotation.

511

512 Figure 10a shows digitized outlines of the iceberg on 8 January 2012 (green), 28 February
513 2012 (pink), 14 June 2012 (blue), and 1 August 2012 (white), stacked chronologically.

514 In this figure, we see that most of the iceberg deterioration occurred on the “southern”

515 side of the iceberg. To quantify this preferential deterioration more precisely, we divide

516 the iceberg into four quadrants, as shown in Fig 10b, and calculate the areal difference

517 between the first (8 January 2012) and last (1 August 2012) iceberg outline for each quad-

518 rant. PII-B-1 experienced 1.8 km^2 of deterioration over the 7.5 months of RADARSAT-2

519 monitoring. The southwest and southeast quadrants accounted for the majority of PII-

520 B-1’s decrease in surface area with 0.47 km^2 and 0.88 km^2 lost over each, respectively.

521 The combined areal deterioration of the southern quadrants represented 75 percent of the

522 iceberg’s total decrease in surface area, while only 27 percent of the iceberg’s perimeter

523 was located within these two quadrants.

524

525 The time-averaged wind direction at the location of PII-B-1, averaged over the entire

526 RADARSAT-2 monitoring period (including the period when the ocean was covered by

527 sea ice) was towards the direction $\theta = 157^\circ$, counterclockwise from east. Here we use the

528 ERA-Interim daily reanalysis wind direction 10 m above the surface. This wind direction

529 implies maximum downwelling (or enhanced stratification at the base of the thermocline)

530 in the direction $\phi = 247^\circ$ counterclockwise from east, which would result in warmest

531 surface waters in this direction. This is broadly consistent with there being a greater

532 deterioration rate on the southern side of the iceberg. The time-averaged wind direction

533 at the location of PII-B-1 from July 4th (when the sea ice began to clear) to the end of the
534 RADARSAT-2 monitoring period, when most of the surface melting is likely to occur, was
535 towards the direction at $\theta = 210^\circ$ counterclockwise from east. This wind direction implies
536 maximum downwelling (or enhanced stratification at the base of the thermocline) in the
537 direction $\phi = 300^\circ$ counterclockwise from east, which is also consistent with increased
538 decay on the southwest quadrant of the iceberg.

539

5. Conclusion

540 Hydrographic data collected around two icebergs in Baffin Bay during three field cam-
541 paigns show asymmetries in the ocean temperature and salinity around the icebergs.
542 Regions of warm and fresh surface water are observed to occur on one side of the ice-
543 berg, while the opposite side is cooler and saltier. An analysis of the data indicates that
544 these asymmetries are likely to be caused by wind-induced ocean upwelling and wind-
545 induced enhanced stratification occurring on opposite sides of the iceberg. Wind-induced
546 upwelling cause the mixed layer to be cooler and more saline on one side of the iceberg,
547 while on the opposing side of the iceberg, the surface winds causes a sharpening of the
548 density gradients at the base of the thermocline causing the mixed layer to be warmer
549 and fresher. Wind data, taken from ERA-Interim reanalysis and in situ measurements,
550 are consistent with this mechanism.

551

552 It is hypothesized that these asymmetries in ocean temperature could lead to preferential
553 deterioration on one side of the iceberg through enhanced melting, as well as through
554 the iceberg footloose mechanism [*Wagner et al.*, 2014]. This suggests that the wind di-

555 rection and speed can significantly influence the rate of degradation around a grounded
556 iceberg. This hypothesis was tested by monitoring the degradation of PII-B-1 over the
557 first 6 months of 2012 using satellite imagery and comparing the results to reanalysis
558 wind data. During this time the iceberg deteriorated primarily on the southern side of
559 the iceberg. This supports the idea that iceberg decay is accelerated by wind-induced
560 enhanced stratification, since the predominant regional winds over the period were from
561 the east.

562

563 **Acknowledgments.** Special thank you to the BBC crew on Operation Iceberg, and
564 the crew of MV Neptune. Information about the television documentary Operation Ice-
565 berg can be found at <http://www.bbc.co.uk/programmes/p00tvcnx>. We would like to
566 acknowledge the following organizations and individuals for the collection of complimen-
567 tary data to that gathered around PII-B-1 in 2012. This includes data from field work
568 in both 2011 and 2013, which was supported by the Canadian Ice Service (Environment
569 Canada; specifically Leah Braithwaite), ArcticNet, and the captain and crew of CCGS
570 *Amundsen*. ArcticNet co-Principle Investigator Derek Mueller is thanked for his sup-
571 port of ice island field work carried out from CCGS *Amundsen* in both 2011 and 2013.
572 The members of the 2011 CCGS *Amundsen* iceberg campaign were Derek Mueller (Car-
573 leton University), Alexander Forrest (U. California Davis-Tahoe), Andrew Hamilton (U.
574 British Columbia), Bernard Laval (U. British Columbia) and Richard Yeo (AUV Con-
575 sultants). Also, thanks to Yves Gratton (From INRS-ETE, Quebec City, Canada) and
576 Pascal Guillot (ISMER-UQAR, Rimouski, Canada) for the quality control of the CTD
577 data. RADARSAT-2 acquisitions were originally acquired for the ice monitoring efforts

578 of analysts at the Canadian Ice Service (Environment Canada) and we thank them for
579 providing this data for our analysis.

References

- 580 Amante, C. and B. W. Eakins (2009), ETOPO1 1 Arc-Minute Global Relief Model: Proce-
581 dures, Data Sources and Analysis. NOAA Technical Memorandum NESDIS NGDC-24.
582 National Geophysical Data Center, NOAA.
- 583 Bakun, A. (1990), Global climate change and intensification of coastal ocean upwelling.
584 *Science*, *247*, 198-201.
- 585 Botsford, L. W., C. A. Lawrence, E. P., Dever, A. Hastings and J. Largier (2003), Wind
586 strength and biological productivity in upwelling systems: an idealized study. *Fisheries*
587 *Oceanography*, *12*, 245-259.
- 588 Botsford, L. W., C. A. Lawrence, E. P., Dever, A. Hastings and J. Largier (2006), Effects
589 of variable winds on biological productivity on continental shelves in coastal upwelling
590 systems. *Deep Sea Res. II: Topical Studies in Oceanogr.*, *53*, 3116-3140.
- 591 Biddle, L. C., J. Kaiser, K. J. Heywood, A. F. Thompson and A. Jenkins (2015), Ocean
592 glider observations of iceberg-enhanced biological productivity in the northwestern Wed-
593 dell Sea. *Geophys. Res. Lett.* doi: 10.1002/2014GL062850
- 594 Bigg, G. R., M. R. Wadley, D. P. Stevens, and J. A. Johnson (1997), Modeling the
595 dynamics and thermodynamics of icebergs. *Cold Regions Science and Technology*, *26*,
596 113-135.
- 597 Braithwaite, R. J. (2009), Calculation of sensible-heat flux over a melting ice surface using
598 simple climate data and daily measurements of ablation. *Ann. Glaciol.*, *50*, 9-15.

- 599 Coogle, R. A. and A. M Howard (2013), The Iceberg Observation Problem: Using Mul-
600 tiple Agents to Monitor and Observe Ablating Target Sources. *In Systems, Man, and*
601 *Cybernetics (SMC), 2013 IEEE International Conference*, 1660-1665.
- 602 Dee, D. P., S. M. Uppala, A. J. Simmons, P. Berrisford, P. Poli, S. Kobayashi, U. Andrae,
603 M. A. Balmaseda, G. Balsamo, P. Bauer, P. Bechtold, A. C. M. Beljaars, L. van de Berg,
604 J. Bidlot, N. Bormann, C. Delsol, R. Dragani, M. Fuentes, A. J. Geer, L., S Haimberger,
605 B. Healy, H. Hersbach, E. V. Hólm, L. Isaksen, P. Kållberg, M. Köhler, M. Matricardi,
606 A. P. McNally, B. M. Monge-Sanz, J.-J. Morcrette, B.-K. Park, C. Peubey, P. de Ros-
607 nay, C. Tavolato, J.-N. Thpaut, and F. Vitart (2011), The ERA-Interim reanalysis:
608 configuration and performance of the data assimilation system. *Q.J.R. Meteorol. Soc.*,
609 *137*, 553-597.
- 610 De Szoeki, R. A. and J. G. Richman (1981), The role of wind-generated mixing in coastal
611 upwelling. *J. Phys. Oceanogr.*, *11*, 1534-1547.
- 612 Dietrich, D. E., M. J. Bowman, C. A. Lin, and A. Mestas-Nunez (1996), Numerical studies
613 of small island wakes in the ocean. *Geophys. Astrophys. Fluid*, *83*, 195-231.
- 614 Dinniman, M. S., J. M. Klinck, and W. O. Smith Jr. (2007), Influence of sea ice cover and
615 icebergs on circulation and water mass formation in a numerical circulation model of
616 the Ross Sea, Antarctica, *J. Geophys. Res.*, **112**, C11013, doi:10.1029/2006JC004036.
- 617 Donaldson, P.B., 1978. Melting of Antarctic icebergs. *Nature* **275**, 305306.
- 618 Ekman, W. K. (1905), On the influence of Earth's rotation on ocean currents. *Ark. Mat.*
619 *Astron. Fys.*, *2*, 1-53.
- 620 Hunke, E. C., and D. Comeau (2011), Sea ice and iceberg dynamic interaction. *J. Geophys.*
621 *Res.*, *116*, C5.

- 622 Falkner, K. K., H. Melling, A. M. Mnchow, J. E. Box, T. Wohlleben, H. L. Johnson, P.
623 Gudmandsen, R. Samelson, L. Copland, K. Steffen, E. Rignot and A. K. Higgins (2011),
624 Context for the Recent Massive Petermann Glacier Calving Event, *Eos Trans. AGU*,
625 *92*,117.
- 626 Gade, H. G. (1979), Melting of ice in sea water: A primitive model with application to
627 the Antarctic ice shelf and icebergs. *J. Phys. Oceanogr.*, *9*, 189-198.
- 628 Garvine, R.W. (1971), A Simple Model of Coastal Upwelling Dynamics. *J. Phys.*
629 *Oceanogr.*, *1*, 169-179.
- 630 Gladstone, R. M., G. R. Bigg, and K. W. Nicholls (2001), Iceberg trajectory modeling and
631 meltwater injection in the Southern Ocean. *J. Geophys. Res* (19782012), *106*, 19903-
632 19915.
- 633 Grosfeld, K., M. Schröder, E. Fahrbach, R. Gerdes, and A. Mackensen (2001), How iceberg
634 calving and grounding change the circulation and hydrography in the Filchner Ice Shelf
635 Ocean System. *J. Geophys. Res*, *106*, 9039-9055.
- 636 Halliday, E. J., T. King, P. Bobby, L. Copland, and D. Mueller (2012), Petermann Ice
637 Island A Survey Results Offshore Labrador. In OTC Arctic Technology Conference.
638 Offshore Technology Conference.
- 639 Helly, J. J., R. S. Kaufmann, G. R. Stephenson Jr., and M. Vernet, (2011a). Cooling,
640 dilution and mixing of ocean water by free-drifting icebergs in the Weddell Sea. *Deep-*
641 *Sea Res PT II*, **58(11-12)**:1346-1363.
- 642 Holland, D.M., and A. Jenkins (1999), Modeling thermodynamic ice-ocean interactions
643 at the base of an ice shelf. *J. Phys. Oceanogr.*, *29*, 1787-1800.

- 644 Hossain, K., and A. R. Rao (2014), Environmental Change And Its Affect. *European*
645 *Journal of Sustainable Development*, *3*, 89-96.
- 646 Hutchins, D. A. and K. W. Bruland (1998), Iron-limited diatom growth and Si: N uptake
647 ratios in a coastal upwelling regime. *Nature*, *393*, 561-564.
- 648 Huppert, H.E. and J. S. Turner, 1980. Ice blocks melting into a salinity gradient. *J. Fluid*
649 *Mech.* **100**, 367384.
- 650 Jakobsson, M., L. A. Mayer, B. Coakley, J. A. Dowdeswell, S. Forbes, B. Fridman, H.
651 Hodnesdal, R. Noormets, R. Pedersen, M. Rebecso, H.-W. Schenke, Y. Zarayskaya A,
652 D. Accettella, A. Armstrong, R. M. Anderson, P. Bienhoff, A. Camerlenghi, I. Church,
653 M. Edwards, J. V. Gardner, J. K. Hall, B. Hell, O. B. Hestvik, Y. Kristoffersen, C.
654 Marcussen, R. Mohammad, D. Mosher, S. V. Nghiem, M. T. Pedrosa, P. G. Travaglini,
655 and P. Weatherall (2012), The International Bathymetric Chart of the Arctic Ocean
656 (IBCAO) Version 3.0, *Geophys. Res. Lett.*, *393*, L12609.
- 657 , Jansen, D., H. Sandhäger, and W. Rack (2005), Model experiments on large tabular
658 iceberg evolution: ablation and strain thinning. *J. Glaciol.*, *51*, 363-372.
- 659 , Jenkins, A. (1999). The impact of melting ice on ocean waters. *J. Phys. Oceanogr.*,
660 **29(9)**, 2370-2381.
- 661 Jongma, J. I., E. Driesschaert, T. Fichefet, H. Goosse, and H. Renssen (2009), The effect of
662 dynamic-thermodynamic icebergs on the Southern Ocean climate in a three-dimensional
663 model. *Ocean Modelling*, *26*, 104-113.
- 664 Kaufmann, R. S., B. H. Robison, R. E. Sherlock, K. R. Reisenbichler, and K. J. Osborn
665 (2011). Composition and structure of macrozooplankton and micronekton communities
666 in the vicinity of free-drifting antarctic icebergs. *Deep-Sea Res PT II*, **58(11-12)**:1469-

- 667 1484.
- 668 Kämpf, J., M. Doubell, D. Griffin, R. L. Matthews, and T. M. Ward (2004), Evidence of a
669 large seasonal coastal upwelling system along the southern shelf of Australia. *Geophys.*
670 *Res. Lett.*, *31*, no. 9.
- 671 Knap, W. H., and J. Oerlemans (1996). The surface albedo of the Greenland ice sheet:
672 Satellite-derived and in situ measurements in the Sondre Stromfjord area during the
673 1991 melt season. *J. Glaciol.*, *42*, 364-674.
- 674 Keghouche, I., L. Bertino, and K. A. Lister (2009), Parameterization of an Iceberg Drift
675 Model in the Barents Sea. *J. Atmos. Oceanic Technol.*, *26*, 2216-2227.
- 676 Kusahara, K., H. Hasumi, and G. D. Williams (2011), Impact of the Mertz Glacier Tongue
677 calving on dense water formation and export. *Nature communications*, *2*, 159.
- 678 Kubat, I., M. Sayed, S. Savage, T. Carrieres, and G. Crocker (2007). An operational ice-
679 berg deterioration model. In Proceedings of the Sixteenth (2007) International Offshore
680 and Polar Engineering Conference, 652-657.
- 681 Martin, T., and A. Adcroft (2010), Parameterizing the fresh-water flux from land ice
682 to ocean with interactive icebergs in a coupled climate model. *Ocean Modelling*, *34*,
683 111-124.
- 684 Martin, S., R. Drucker, R. Aster, and F. Davey (2010), Kinematic and seismic analysis of
685 giant tabular iceberg breakup at Cape Adare, Antarctica. *J. Geophys. Res.*, *115*, B6.
- 686 McDougall, T.J. and P.M. Barker (2011), Getting started with TEOS-10 and the Gibbs
687 Seawater (GSW) Oceanographic Toolbox, 28pp., SCOR/IAPSO WG127, ISBN 978-0-
688 646-55621-5.

- 689 McPhee, M. G. (1992), Turbulent heat flux in the upper ocean under sea ice. *J. Geophys.*
690 *Res.*, *97*, 5365-5379.
- 691 McPhee, M.G. (2008), Air-Ice-Ocean Interaction: Turbulent Ocean Boundary Layer Ex-
692 change Processes. ISBN 978-0-387-78334-5, Chapter 6, Springer.
- 693 Nøst, O. A., and S. Østerhus (1998), Impact of grounded icebergs on the hydrographic
694 conditions near the Filchner Ice Shelf. *Ocean, Ice, and Atmosphere: Interactions at the*
695 *Antarctic Continental Margin*, 267-284.
- 696 Newell, J. P. (1993), Exceptionally large icebergs and ice islands in eastern Canadian
697 waters: a review of sightings from 1900 to present. *Arctic*, 205-211.
- 698 Neshyba, S. (1977), Upwelling by icebergs. *Nature*, 507-508
- 699 Padman, L., and S. Erofeeva (2004), A barotropic inverse tidal model for the Arctic Ocean.
700 *Geophys. Res. Lett.*, *31*, no. 2.
- 701 Paterson, W. S. B (1994), The physics of glaciers, 3rd edition, Butterworth-Heinemann,
702 Oxford, U. K.
- 703 Peterson, I. K., J. S. Holladay, and L. Lalumiere (2012). Labrador Shelf Pack Ice and
704 Iceberg Survey, *March 2011*. Fisheries and Oceans Canada.
- 705 Price, J. F., R. A. Weller, and R. R. Schudlich (1987), Wind-driven ocean currents and
706 Ekman transport. *Science*, *238*, 1534-1538.
- 707 Rignot, E., S. Jacobs, J. Mouginot, and B. Scheuchl (2013), Ice-shelf melting around
708 Antarctica. *Science*, *341*, 266-270.
- 709 Robinson, N. J., M. J. M. Williams, P. J. Barrett, and A. R. Pyne (2010), Observations of
710 flow and ice-ocean interaction beneath the McMurdo Ice Shelf, Antarctica. *J. Geophys.*
711 *Res*, *115*.

- 712 N.J. Robinson and M.J.M. Williams (2012), Iceberg-induced changes to polynya oper-
713 ation and regional oceanography in the southern Ross Sea, Antarctica, from in situ
714 observations. *Antarctic Science*, **24**, pp 514-526. doi:10.1017/S0954102012000296.
- 715 Rolstad, C., and J. Oerlemans (2005), The residual method for determination of the
716 turbulent exchange coefficient applied to automatic weather station data from Iceland,
717 Switzerland and West Greenland. *Ann. Glaciol.*, *42*, 367-372.
- 718 Rye, C. D., A. C. N. Garabato, P. R. Holland, M. P. Meredith, A. G. Nurser, C. W.
719 Hughes, A.C. Coward, and D.J. Webb (2014). Rapid sea-level rise along the Antarctic
720 margins in response to increased glacial discharge. *Nature Geoscience*, *7*, 732-735.
- 721 Savage, S. B. (2001), Aspects of iceberg deterioration and drift, in Geomorphological
722 Fluid Mechanics, Lect. Notes Phys. Ser., vol. 582, edited by N. J. Balmforth, and A.
723 Provenzale, pp. 279-318, Springer, Berlin.
- 724 Scambos, T., O. Sergienko, A. Sargent, D. MacAyeal, and J. Fastook (2005), ICESat
725 profiles of tabular iceberg margins and iceberg breakup at low latitudes. *Geophys. Res.*
726 *Lett.*, *32*, no. 23.
- 727 Send, U., R. C. Beardsley, and C. D. Winant (1987), Relaxation from upwelling in the
728 coastal ocean dynamics experiment. *J. Geophys. Res.*, *92*, 1683-1698.
- 729 Shaw, T. J., R. Raiswell, C. R. Hexel, H. P. Vu, W. S. Moore, R. Dudgeon, and K. L.
730 Smith Jr. (2011). Input, composition, and potential impact of terrigenous material from
731 free-drifting icebergs in the Weddell Sea. *Deep-Sea Res PT II*, **58(11-12)**:1376-1383.
- 732 Silva, T. A. M., G. R. Bigg, and K. W. Nicholls (2006), Contribution of giant icebergs to
733 the Southern Ocean freshwater flux. *J. Geophys. Res.*, *111*, C3.

- 734 Smith, L. C., and S. R. Stephenson (2013), New Trans-Arctic shipping routes navigable
735 by midcentury. *P. Nat. Aca. of Sci.*, *110*, E1191-E1195.
- 736 Smith, K., B. Robison, J. Helly, R. Kaufmann, H. Ruhl, H., T. Shaw, and M. Vernet,
737 (2007). Free-drifting icebergs: hotspots of chemical and biological enrichment in the
738 Weddell Sea. *Science*, **317**
- 739 Smith, Jr., K. L. (2011). Free-drifting icebergs in the Southern Ocean: An overview.
740 *Deep-Sea Res PT II*, **58(11-12)**:1277-1284.
- 741 Smith, S.D., (1980) Wind Stress and Heat Flux over the Ocean in Gale Force Winds. *J.*
742 *Phys. Oceanogr.*, *10*, 709-726.
- 743 Stern, A. A., M. S. Dinniman, V. Zagorodnov, S. W. Tyler, and D. M. Holland (2013),
744 Intrusion of warm surface water beneath the McMurdo Ice Shelf, Antarctica. *J. Geophys.*
745 *Res.*, *118*, 7036-7048.
- 746 Stephenson, Jr., G. R., J. Sprintall, S. T. Gille, M. Vernet, J. J. Helly and R. S. Kaufmann
747 (2011). Subsurface melting of a free-floating Antarctic iceberg. *Deep-Sea Res PT II*,
748 **58(11-12)**:1336-1345.
- 749 Takahashi, M., I. Koike, T. Ishimaru, T. Saino, K. Furuya, Y. Fujita, A. Hattori, and
750 S.E. Ichimura (1980), Upwelling plumes in Sagami Bay and adjacent water around the
751 Izu Islands, Japan. *J. Oceanographical Society of Japan*, *36*, 209-216.
- 752 Turnbull, I. D., N. Fournier, M. Stolwijk, T. Fosnaes, and D. McGonigal (2015). Opera-
753 tional iceberg drift forecasting in Northwest Greenland. *Cold Reg. Sci. Technol.*, **110**,
754 1-18.
- 755 Van de Wal, R. S. W., and A. J. Russell (1994), A comparison of energy balance calcula-
756 tions, measured ablation and meltwater runoff near Søndre Strømfjord, West Greenland.

- 757 *Global and planetary change*, 9, 29-38.
- 758 Vernet, M., K. Sines, D. Chakos, A. O. Cefarelli, and L. Ekern, (2011). Impacts on
759 phytoplankton dynamics by free-drifting icebergs in the NW Weddell Sea. *Deep-Sea*
760 *Res PT II*, **58(11-12)**:1422-1435.
- 761 Vernet, M., K.L. Smith Jr., A.O. Cefarelli, J.J. Helly, R.S. Kaufmann, H. Lin, D.G. Long,
762 A.E. Murray, B.H. Robison, H.A. Ruhl, T.J. Shaw, A.D. Sherman, J. Sprintall, G.R.
763 Stephenson Jr., K.M. Stuart, and B.S. Twining (2012), Islands of Ice: Influence of
764 Free-Drifting Antarctic Icebergs on Pelagic Marine Ecosystems. *Oceanography*, **25(3)**:
765 38-39.
- 766 Wadhams, P., M. Kristensen, and O. Orheim (1983). The response of Antarctic icebergs
767 to ocean waves. *J. Geophys. Res.*, 88, 6053-6065.
- 768 Wagner T. J. W., P. Wadhams, R. Bates, P. Elosegui, A.A. Stern, D. Vella, E. P. Abra-
769 hamsen, A. Crawford, and K. W. Nicholls (2014), The “footloose” mechanism: iceberg
770 decay from hydrostatic stresses. *Geophys. Res. Letters*, 41, 5522-5529.
- 771 White, F. M., M. L. Spaulding, and L. Gominho (1980), Theoretical estimates of the
772 various mechanisms involved in iceberg deterioration in the open ocean environment.
773 *Tech. Rep. USCG-D-62-80*.
- 774 White, L., E. Deleersnijder, and V. Legat (2008), A three-dimensional unstructured mesh
775 finite element shallow-water model, with application to the flows around an island and
776 in a wind-driven, elongated basin. *Ocean Modelling*, 22, 26-47.
- 777 Wolanski, E., T. Asaeda, A. Tanaka, and E. Deleersnijder (1996). Three-dimensional
778 island wakes in the field, laboratory experiments and numerical models. *Continental*
779 *Shelf Research*, 16, 1437-1452.

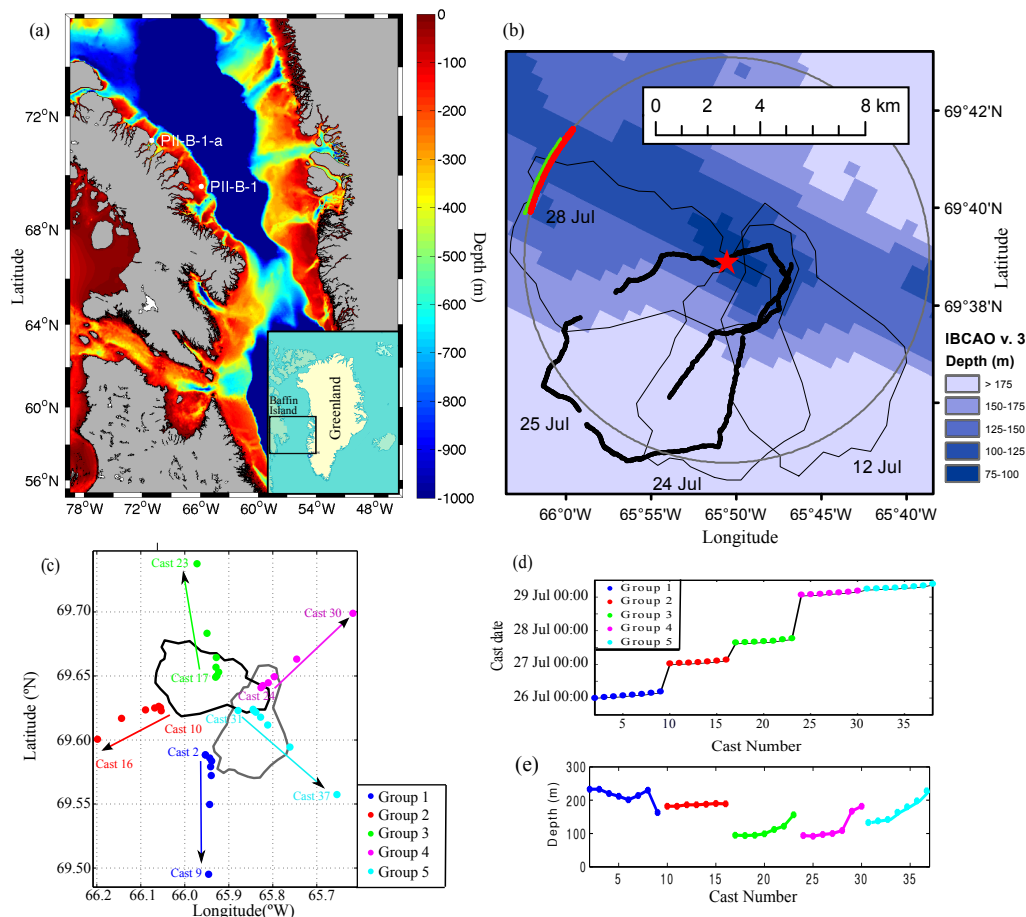


Figure 1. (a) Regional bathymetry in Baffin Bay taken from the ETOPO1 data set [Amante and Eakins, 2009]. The position of PII-B-1 and PII-B-a are shown. (b) Local bathymetry around PII-B-1, taken from IBCAO V3 [Jakobsson *et al.*, 2012]. Red and green curves show the position of the GPS units which were deployed on PII-B-1. Outlines of the iceberg, traced from MODIS satellite images from 12 July 2012, 24 July 2012 and 28 July 2012, are shown with thin black lines. The thick black line is from the first lidar survey of the iceberg on 25 July 2012; the iceberg rotated during the survey, so the line is not closed. A circle is plotted around the point marked with a star, which is approximately the point where the iceberg was grounded. (c) Positions, (d) times, and (e) depths of CTD casts collected around PII-B-1 during the July 2012 survey. MODIS images from 24 July 2012 and 28 July 2012 also are shown in panel (c).

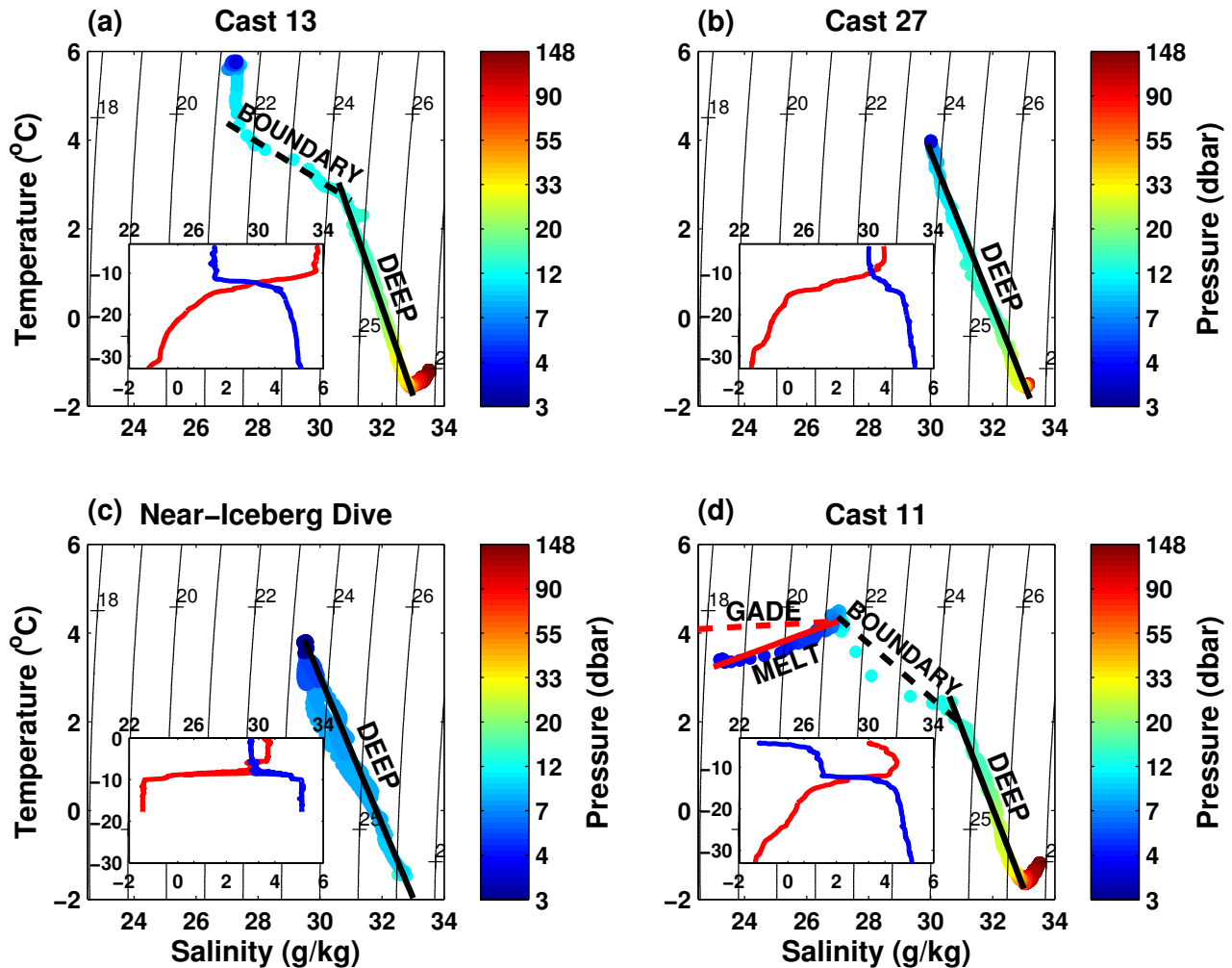


Figure 2. Panels (a), (b) and (d) show the T-S diagram for Cast 13 (Group 2), Cast 27 (Group 4) and Cast 11 (Group 2), respectively. The colors of the plots indicate the pressure at which the measurements were made. Panel (c) shows the T-S diagram for a cast made within a few centimeters of the iceberg edge. The T-S diagrams in all four panels have been fitted with straight lines which indicated the mixing lines (see text). The inset in each panel shows the temperature and absolute salinity profiles of the cast. All data in this figure were collected in July 2012 around PII-B-1.

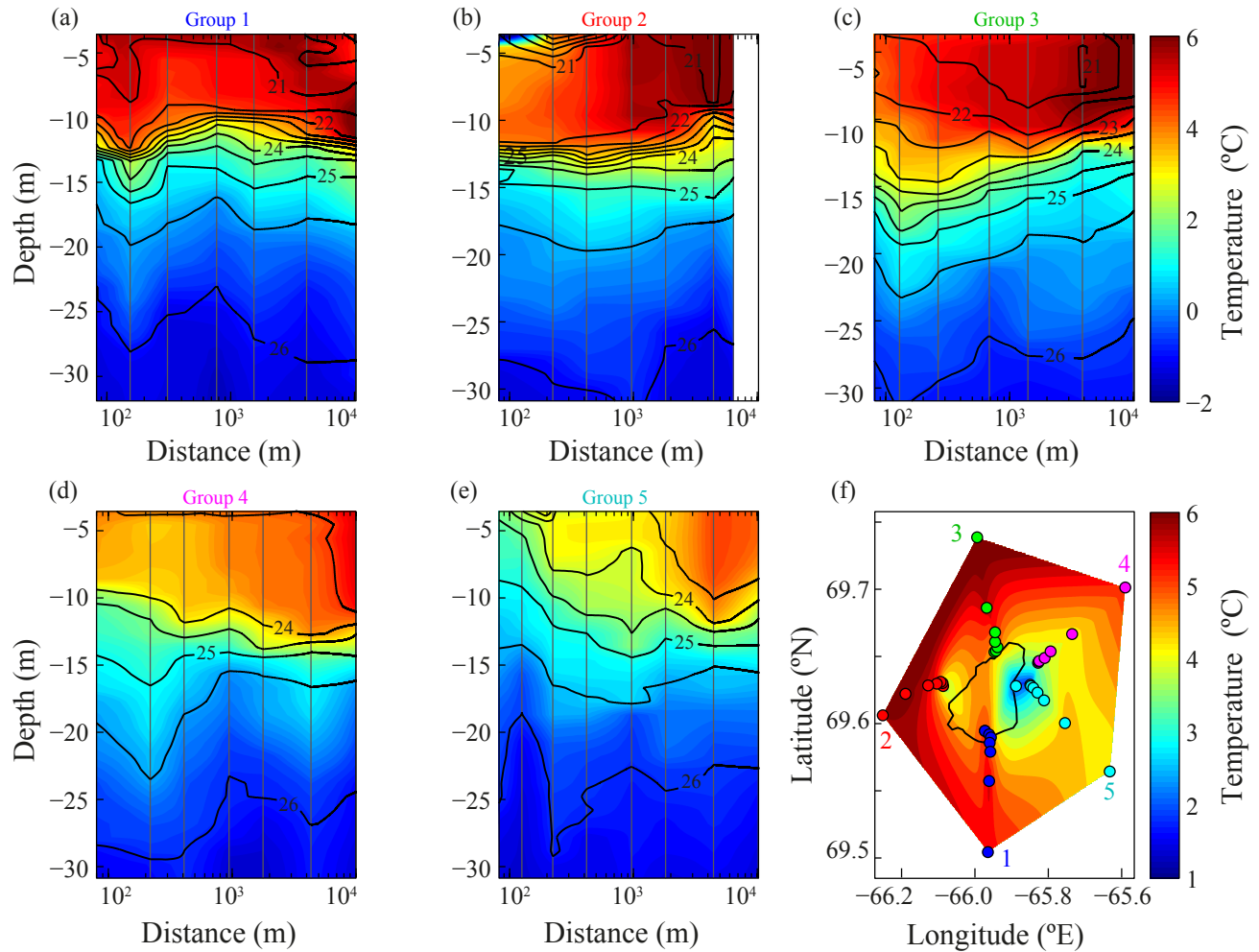


Figure 3. Panels (a) to (e) show the temperature sections around PII-B-1 collected in July 2012 in Group 1 to Group 5, respectively. The vertical axis shows depth below sea level, and the horizontal axis shows distance from the iceberg on a logarithmic scale. Density contours are overlaid. The position of each cast is shown by the vertical grey lines. Panel (f) shows an interpolation of the ocean temperature around PII-B-1 collected in July 2012, at 5 m below the surface. The position of the casts in each group is shown by the colored circles in panel (f).

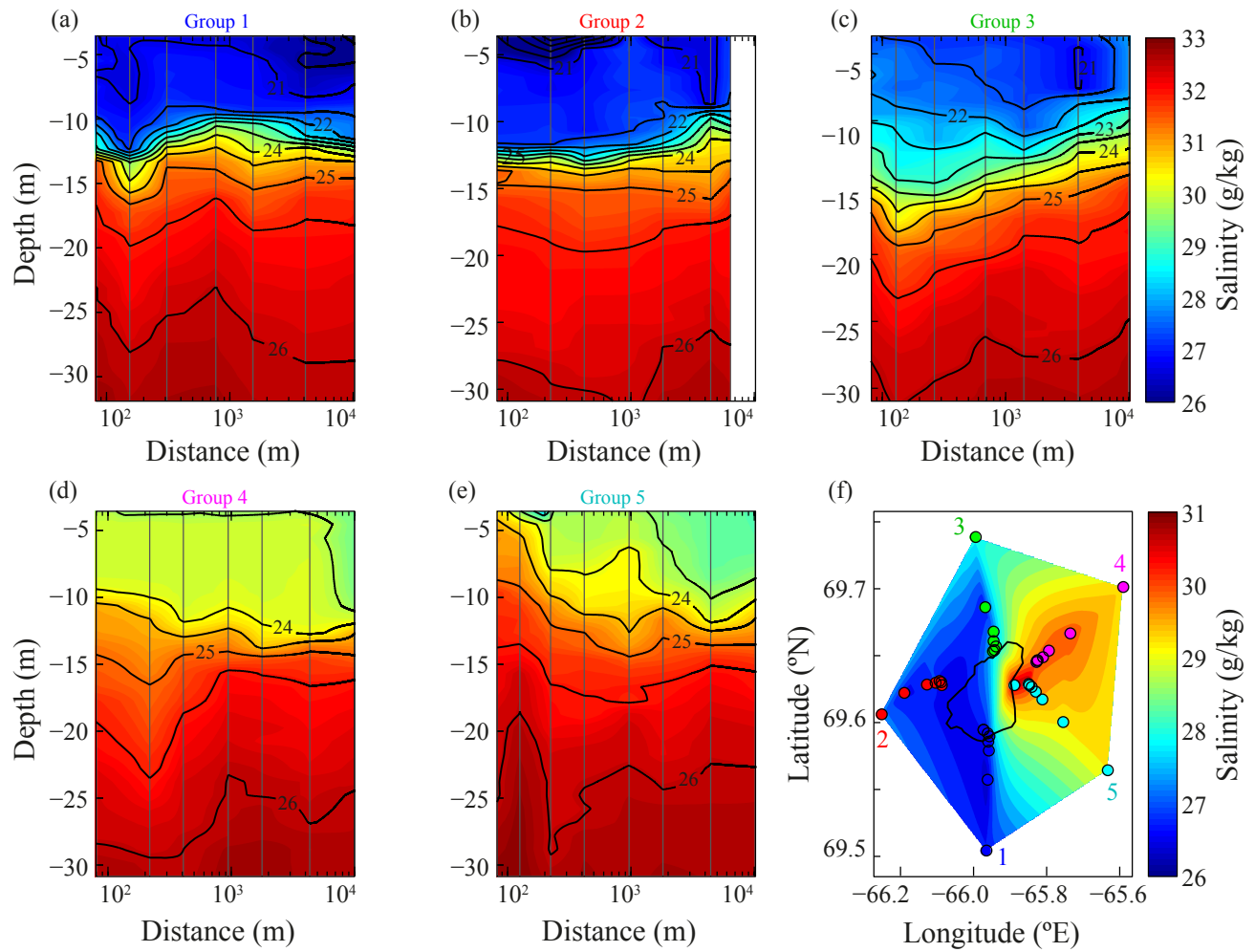


Figure 4. As for Figure 3, but with absolute salinity instead of temperature.

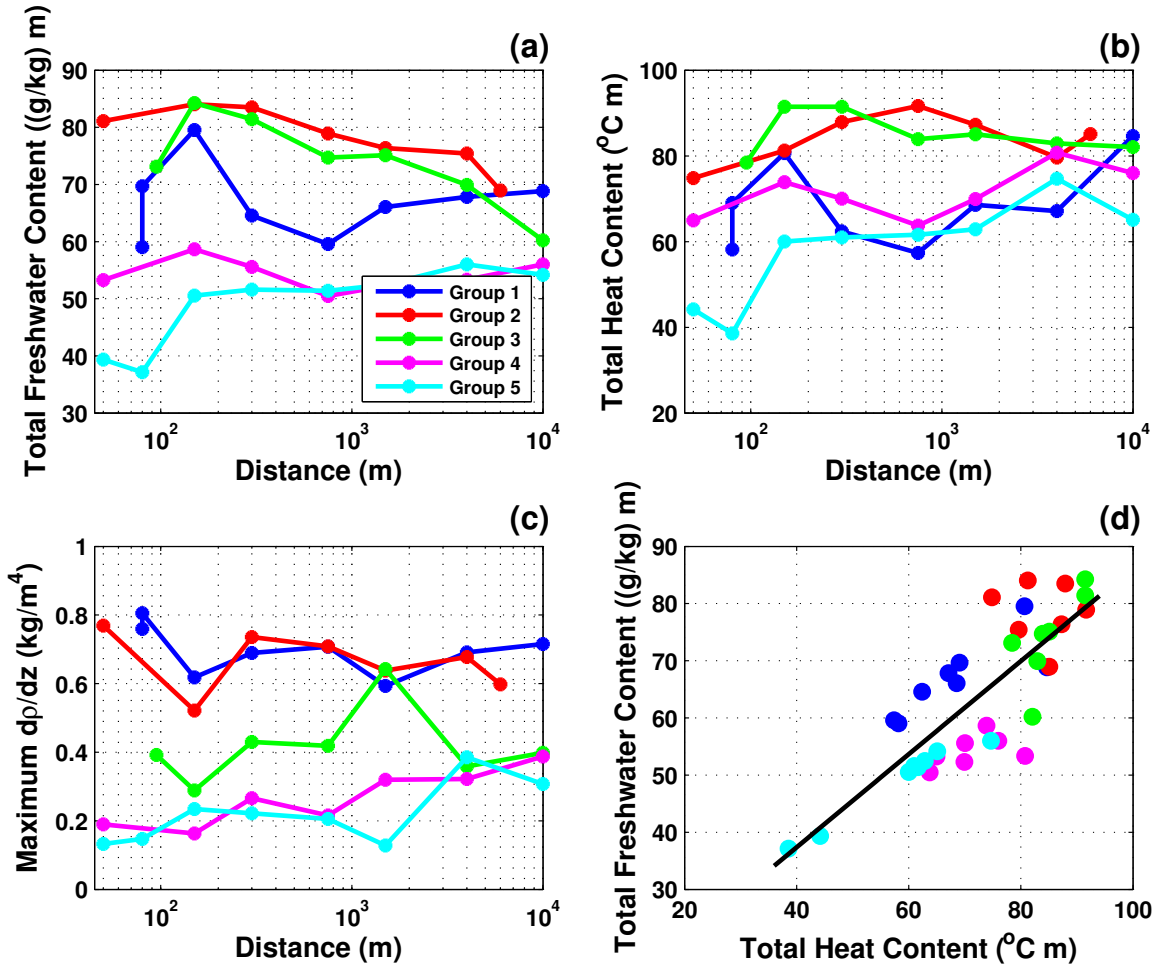


Figure 5. Panels (a), (b) and (c) show how properties of the water column change with distance from PII-B-1 in July 2012: (a) vertically integrated freshwater content, (b) vertically integrated heat content, (c) maximum vertical density gradient in the water column. (d) The relationship between freshwater content and heat content for the different casts.

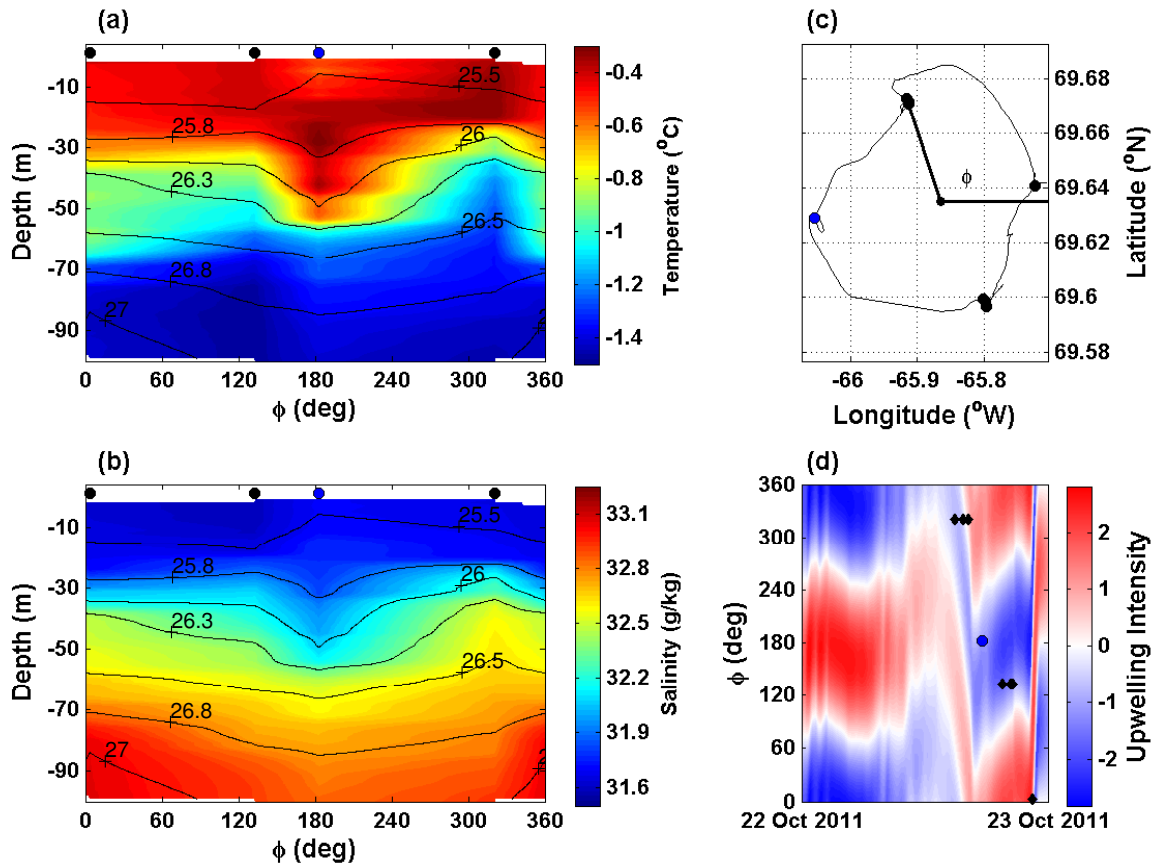


Figure 6. (a) Temperature and (b) absolute salinity sections around PII-B-1, collected in October 2011, with density contours are overlain. (c) The position of CTD casts and the ship's route around the iceberg. (d) Hovmöller diagram of the quantity $C(\phi, t)$. The position of each cast is plotted on the Hovmöller diagram. A blue dot has been used to indicate the position and times of the downwelling cast in all four panels.

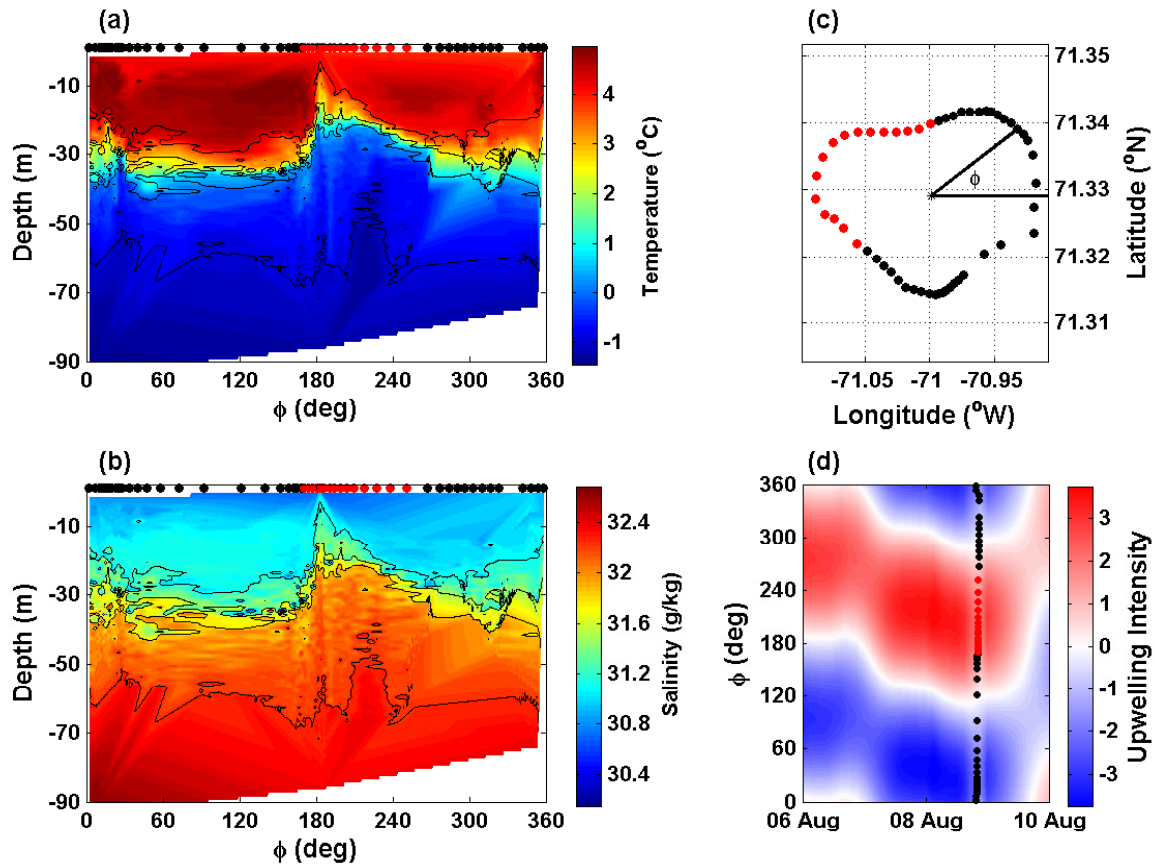


Figure 7. As for Figure 6, but for measurements around iceberg PII-B-a in August 2013. Panel (d) is created using the ERA-Interim reanalysis wind data at 10 m above the surface, and has a 3 hour time resolution. The density contours in panels (a) and (b) are in the range 23.9 to 26.2 kg/m^3

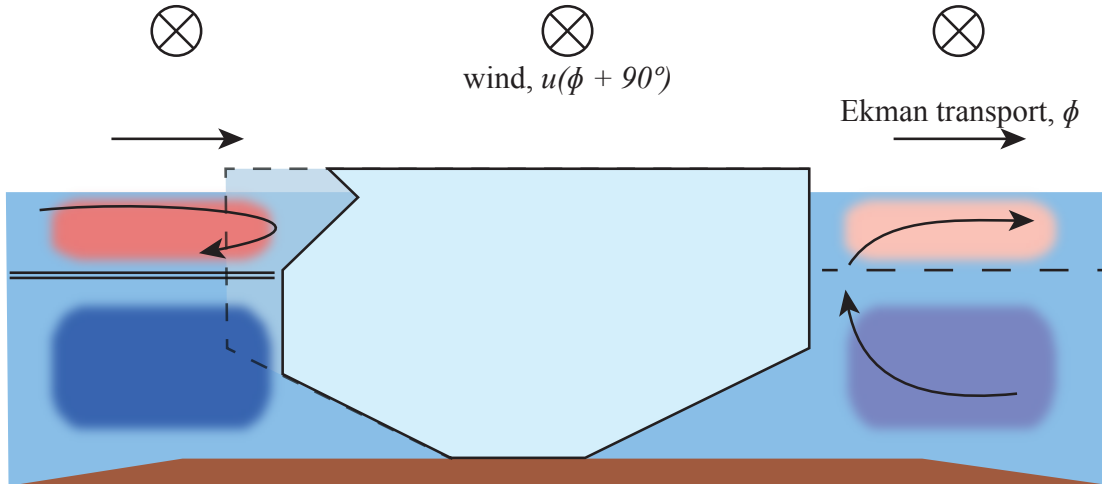


Figure 8. Schematic of the mechanism causing asymmetries in the mixed layer around the grounded icebergs. Surface transport away from the iceberg to the right of the wind direction (in the northern hemisphere) causes upwelling on this side of the iceberg. The upwelling water causes the mixed layer to become cooler and more saline. On the opposite side of the iceberg (to the left of the wind direction in the northern hemisphere), the wind drives a surface transport towards the iceberg. Warm fresh water piles up against the iceberg, which causes a sharpening of the gradients at the base of the thermocline. This causes the mixed layer to be anomalously warm and fresh on this side of the iceberg. The warm fresh water in the thermocline drives preferential deterioration on this side of the iceberg through surface melting, and as a knock on effect through the footloose mechanism [*Wagner et al.*, 2014].

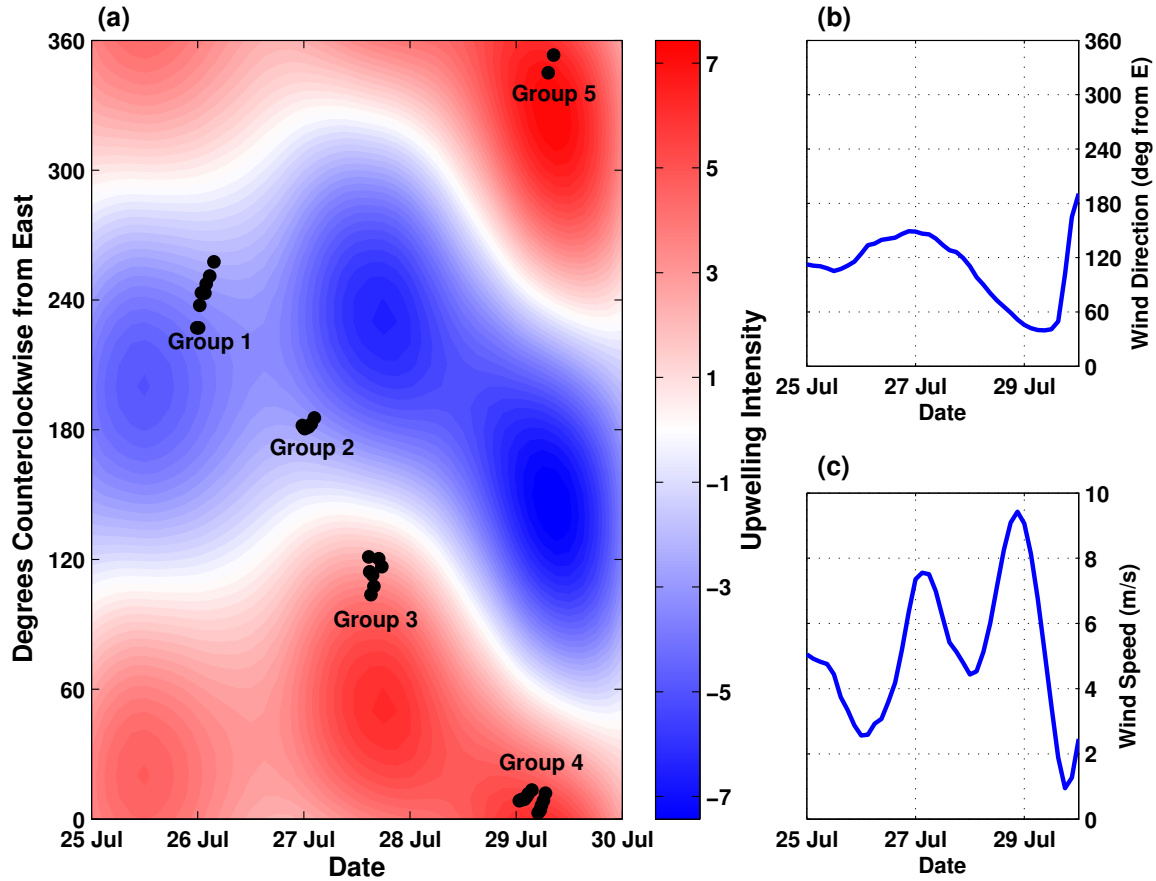


Figure 9. (a) Hovmöller diagram of the quantity $C(\phi, t)$, where ϕ is the angle of rotation counterclockwise from due east. $C(\phi, t)$, defined in the main text, gives a measure of the average amount of upwelling and downwelling around PII-B-1 in July 2012, which has occurred in the direction ϕ over the 24 hours preceding time t , with positive values implying upwelling wind and negative values implying downwelling winds. The position of each cast is plotted on the Hovmöller diagram. The (b) wind angle and (c) wind direction are shown. The wind data is from the ERA-Interim reanalysis product and has a 3 hour time resolution.

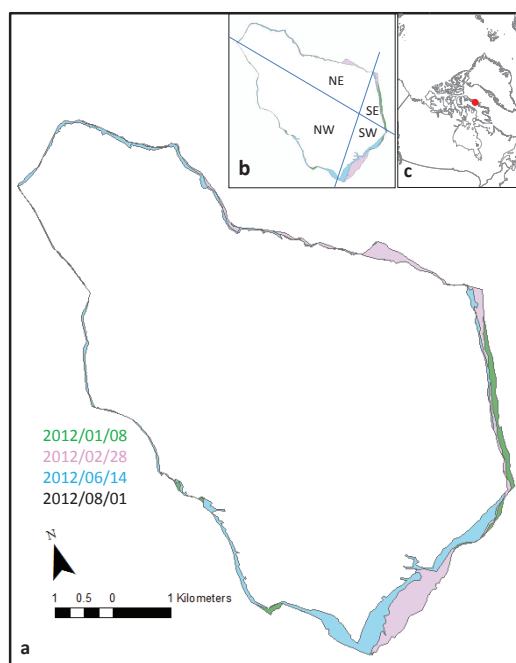


Figure 10. (a) Areal deterioration of PII-B-1 during 2012 as determined through digitization of RADARSAT-2 Fine-Quad imagery. (b) Quadrants used for preferential deterioration assessment. (c) The location of PII-B-1 marked by the red dot.